

www.acsami.org Research Article

Sustainable Enhanced Sodium-Ion Storage at Subzero Temperature with LiF Integration

Heramba Venkata Sai Rama Murthy Koppisetti, Harsha Rao, Hari Vignesh Ramasamy, Harish Reddy Inta, Sayan Das, Soohwan Kim, Yizhi Zhang, Haiyan Wang, Venkataramanan Mahalingam, and Vilas G. Pol*



Cite This: ACS Appl. Mater. Interfaces 2023, 15, 32291-32300



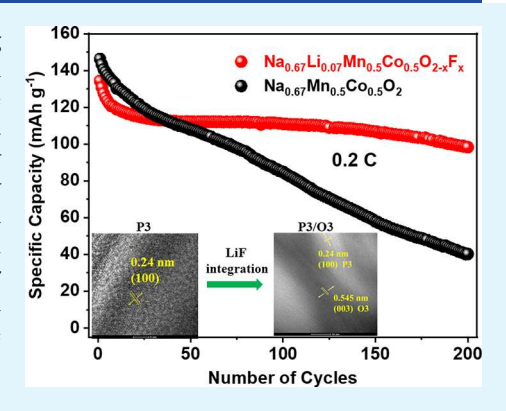
ACCESS

III Metrics & More

Article Recommendations

s Supporting Information

ABSTRACT: Though layered sodium oxide materials are identified as promising cathodes in sodium-ion batteries, biphasic P3/O3 depicts improved electrochemical performance and structural stability. Herein, a coexistent P3/O3 biphasic cathode material was synthesized with "LiF" integration, verified with X-ray diffraction and Rietveld refinement analysis. Furthermore, the presence of Li and F was deduced by inductively coupled plasma-optical emission spectrometry (ICP-OES) and energy dispersive X-ray spectroscopy (EDS). The biphasic P3/O3 cathode displayed an excellent capacity retention of 85% after 100 cycles (0.2C/30 mA g⁻¹) at room temperature and 94% at -20 °C after 100 cycles (0.1C/15 mA g⁻¹) with superior rate capability as compared to the pristine cathode. Furthermore, a full cell comprising a hard carbon anode and a biphasic cathode with 1 M NaPF₆ electrolyte displayed excellent cyclic stabilities at a wider temperature range of -20 to 50 °C (with the energy density of 151.48 Wh kg⁻¹) due to the enhanced structural stability, alleviated Jahn-Teller distortions, and rapid Na⁺ kinetics facilitating Na⁺ motion at



various temperatures in sodium-ion batteries. The detailed post-characterization studies revealed that the incorporation of LiF accounts for facile Na⁺ kinetics, boosting the overall Na storage.

KEYWORDS: LiF incorporation, sodium storage, layered oxide, biphasic cathode, wide temperature

■ INTRODUCTION

The quest for efficient alternative energy storage systems is obligatory due to the intermittent nature of current energy storage systems such as lithium. 1-3 Earth-abundant sodium is considered as the next sodium-ion battery (SIB) technology not only for its lower cost but also for the ease of recyclability and enhanced extreme temperature performance compared to its lithium-ion counterparts.^{4–8} Designing novel host structures plays a pivotal role in developing high-performance SIBs with high capacity and longer cyclic stability.9,10 Furthermore, considering the sustainable solar and wind storage in SIBs, it shall be operational at lower temperatures. 11,12 However, due to the larger size of the Na⁺ (1.02 Å) ion, the extraction and insertion of the Na⁺ ion during the charge and discharge processes result in structural changes, thus affecting the cyclic stability and rate performances of the cathode materials. Among the different reported cathode materials, layered transition-metal oxide (Na_xTMO₂; $0 < x \le 1$, TM——transition metal)-based materials are the state-of-the-art cathodes for SIBs, providing stable cycling and rate performance, incorporating large Na⁺ (1.02 Å) during charge/discharge. 15,16

The layered oxides can be majorly classified into P2, P3, and O3 based on the coordination environment with the content of the alkali metal and the number of TMO₂ layers in the unit

cell. In general, the P- and O-type structures represent prismatic and octahedral coordination around the Na ion, respectively. The adjoining numbers 2 and 3 indicate different arrangements of transition-metal layers in a single unit cell.¹⁷ Among these, P2- and O3- layered oxides are widely studied cathodes due to easy synthesis protocols like controlling the stoichiometry and reaction conditions. 15 P2-type cathodes provide good rate capability and cycle life, whereas O3 delivers a higher initial capacity. However, all these layered structures suffer from multiple phase transitions and decreased capacity during long-term cycling. 18,19 Consequently, it is highly desired to develop cathodes with optimized composition for improved cycle life and higher capacities. 11 Several techniques like the integration of multiple phases and tuning the metal composition or incorporation of structure-stabilizing elements had already been proved to be very effective in improving the

Received: March 8, 2023 Accepted: June 18, 2023 Published: June 28, 2023





electrochemical performance.^{20–22} For instance, Feng et al. explored the performance of a P2/O3 composite cathode (Na_{0.8}Li_{0.13}Ni_{0.2}Fe_{0.1}Mn_{0.57}O₂), which delivered a capacity of 133.4 mAh g⁻¹ at a high rate of 1C and a capacity retention of 88.6% after 100 cycles.²³ Additionally, the inexpensive, low-toxic manganese-based cathodes are highly advisable, but the Jahn–Teller distortion caused by the Mn³⁺ ions results in the appearance of multiple voltage steps in the discharge curve, and the eventual capacity fade leads to further optimization of cathode compositions.²⁴

Recently, synergistic effects on biphasic cathodes which can be synthesized by controlling the reaction conditions, doping elements like Li, Mg, Al, Ti, Mn, Co, Fe, etc., have been demonstrated with improved electrochemical performance. $^{25-28}$ An integrated P2/O3 $Na_{0.66}Li_{0.18}Mn_{0.71}Ni_{0.21}Co_{0.08}O_{2+\delta}$ cathode was reported by Guo et al., demonstrating superior sodium storage ability.² It is important to regulate the Mn valence to suppress the Jahn-Teller effect in layered manganese-based cathodes. Li inclusion into Mn-based layered oxide cathodes is reported to suppress the Jahn-Teller effect by regulating the Mn valence and delaying the phase transformations, resulting in prolonged cycling life. 30 The substitution of Li can potentially help to suppress the Jahn-Teller effect by oxidizing Mn³⁺ to Mn⁴⁺. A recent study by Li et al. with the Na_{0.95}Li_{0.15}Ni_{0.25}Mn_{0.6}O₂ cathode manifests improved electrochemical performance compared to the pristine material.³¹ Furthermore, Liu et al., using a Li/F codoping route, established a mixed P2/O3 cathode which possesses better electrochemical performance than the individual P2 and O3 phases.³² Fluorine substitution has been reported to be effective in addressing the oxygen loss issue in Na-based transition-metal oxides for improved cyclic stability.33,34 Additionally, doping with more electronegative F ions accounts for stronger TM-O(F), which can minimize the gliding of the TMO₂ layers, thus making the layered structure more stable.

Currently, major research on cathode materials is focused on ambient temperature, but very few reports are on SIB operable extreme conditions, specifically low temperature. The specific capacities and rate capabilities greatly reduce with the transition from room temperature to low temperatures due to the sluggish Na⁺ diffusion processes at subzero temperatures. 6,35 Wang et al. performed structural modifications to layered $Na_{0.67}Ni_{0.33}Mn_{0.67}O_2$ (specific capacity of 173 mAh g⁻¹ at 0.2 C) by cobalt substitution, resulting in Na_{0.67}Ni_{0.2}Co_{0.2}Mn_{0.6}O₂, with 132.2 mA h g⁻¹ capacity at -40 ° C (80% retainment in the initial room-temperature capacity). ³⁶ A similar strategy with electrochemically active Fe3+ ions in the Mn site of the P2 layer oxide cathode optimized as Na_{2/3}Ni_{1/3}Mn_{7/12}Fe_{1/12}O₂ exhibits a better lowtemperature performance with a capacity retention of 94% after 80 cycles at -25 °C.³⁷ Recently, lithium-composed layered oxide cathodes with stable structures have been employed at 0 °C for sodium storage. 6 The strategic inclusion of foreign elements into layered oxide cathodes resulted in faster Na+ transfer kinetics and ameliorated sodium storage properties at low temperatures. Therefore, it is highly envisaged to develop structurally stable and high-performance electrodes operable in extreme conditions, specifically subzero temperature.

In this work, we have synthesized a new P3/O3 biphasic cathode by facile LiF codoping into $Na_{0.67}Mn_{0.5}Co_{0.5}O_2$ as $Na_{0.67}Li_{0.07}Mn_{0.5}Co_{0.5}O_{2-x}F_x$ and $Na_{0.67}Li_{0.13}Mn_{0.5}Co_{0.5}O_{2-y}F_y$

through sol-gel synthesis, followed by a high-temperature calcination step. The LiF integration into Na_{0.67}Mn_{0.5}Co_{0.5}O₂ has led to the growth of a biphasic P3/O3 cathode, which is confirmed by XRD and Rietveld analyses. Moreover, the Jahn-Teller distortion from Mn3+ is greatly suppressed with an increased Mn⁴⁺/Mn³⁺ ratio, as confirmed by XPS analysis. At ambient temperature, the optimized cathode exhibits a capacity retention of \sim 85% after 100 cycles at 0.2 C (30 mA g⁻¹) rate compared to the 54% retention of the pristine cathode. Moreover, low-temperature performance at −20 °C gave 70% (92 mAh g^{-1} at 0.1 C/15 mA g^{-1}) of the room-temperature capacity, with 94% capacity retention after 100 cycles. Further, excellent capacity retention in a full-cell configuration, with hard carbon as an anode, has been demonstrated at a wider temperature range of -20 to 50 °C (with an energy density of 151.48 Wh kg⁻¹). The Na⁺ kinetic and postcharacterization studies reveal that the incorporation of LiF accounts for boosting the electrochemical performance.

EXPERIMENTAL SECTION

Materials. The chemicals sodium acetate and lithium fluoride are procured from Alfa Aesar, and anhydrous manganese(II) acetate and cobalt(II) acetate are obtained from Fisher Chemicals. Sodium hexafluorophosphate (NaPF₆, Alfa Aesar) was dissolved in propylene carbonate (PC, Sigma) as the electrolyte.

Synthesis of NMC and LiF-Incorporated NMC Cathode Materials. The $Na_{0.67}Co_{0.5}Mn_{0.5}O_2$ material was synthesized using a simple sol-gel method, followed by high-temperature calcination. Initially, stoichiometric amounts of metal (Na, Co, and Mn) acetates were dissolved in DI water along with citric acid and heated at 90 °C for 12 h to obtain a gel-like compound. Subsequently, the gel was dried at 120 °C to obtain the precursor material. Further, the precursor was sintered at 500 °C for 6 h. Finally, the precalcined material was further annealed at 800 °C for 15 h to obtain the final product. A similar procedure was used to obtain Li-F-incorporated samples Na_{0.67}Li_{0.07}Mn_{0.5}Co_{0.5}O_{2-x}F_x and $Na_{0.67}Li_{0.13}Mn_{0.5}Co_{0.5}O_{2-y}F_y$ by additionally taking LiF in the first step, 10 and 20% moles of Na source were used for NMC-L1 and L2 samples, respectively. Both Na and Li precursors were taken in 5% excess quantity to account for the mass loss during high-temperature annealing. The obtained final products were used for further characterization.

Structural Characterization. The elemental composition was determined using an inductively coupled plasma optical emission spectrometer. The PXRD patterns of the layered oxide cathodes were collected using a Rigaku Smart Lab X-ray diffractometer with a tube voltage of 40 kV and current of 44 mA. Cu K α radiation source was used with a wavelength of 0.154 nm, and the scan range was set from 2-theta values of 10–70°. Further, for morphology analysis, an FEI Tecnai F20 S/transmission electron microscope and an FEI Nova NanoSEM field emission spectroscope were employed. XPS acquisition was done using a Kratos Axis ultra-DLD imaging XPS instrument. The XPS analysis was performed using CASA XPS fitting software, with the C 1s reference set at 284.6 eV and Shirley background. Majority of graphs were plotted using the Origin Pro 2022 software.

Electrochemical Testing. The active materials (80%), super P carbon (10%), and PVDF (10%) were taken with an appropriate amount of N-methyl-2-pyrrolidone (NMP) and mechanically mixed to obtain a uniform slurry. The slurry was further coated on the top of the aluminum current collector using the doctor blade technique and dried overnight at 100 °C in a vacuum oven. The dried foil was then punched into circular disks of diameter 12 mm with a mass loading of 2-3 mg cm $^{-2}$ and further used as cathodes. For the half-cells, the sodium metal foils rolled and cut into disks were used as anodes, and 1 M NaPF₆ in propylene carbonate (PC) was used as the electrolyte, while glass microfiber filters (Whatman-grade GF/D) served as the separator. The full cells were assembled with hard carbon (Kuranode

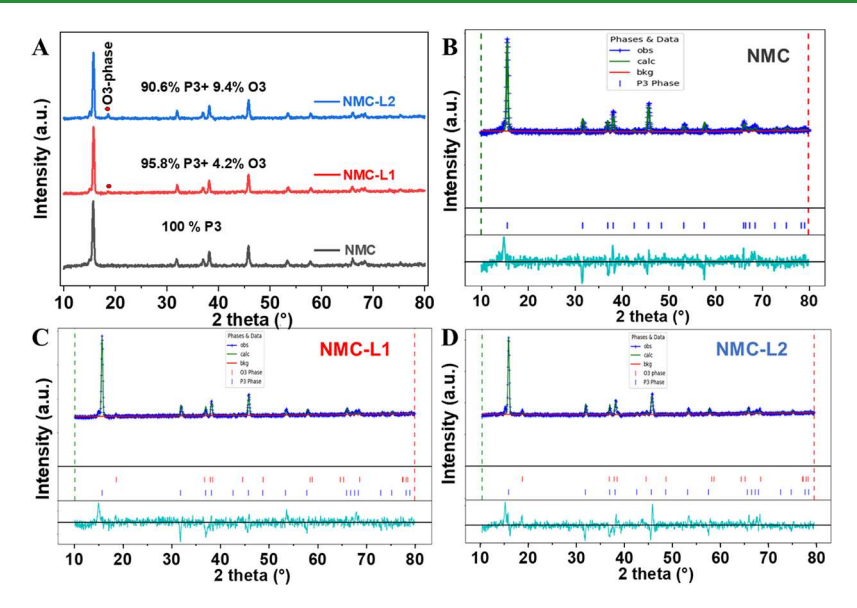


Figure 1. (A) PXRD patterns and (B-D) Rietveld refinement analyses of NMC and NMC-L1 and L2 samples, respectively.

hard carbon powder, Kuraray). To prepare the negative carbon electrodes, a slurry of 80 wt % HC and 10 wt % each of super P carbon and PVDF in NMP was cast onto a copper current collector. The mass of the cathode and anode was taken in 10:8 ratio. CR 2032type coin cells were subsequently assembled with the above components in an Ar-filled glovebox and tested with MTI and Arbin battery cyclers. The electrolyte composition remained unchanged for both room-temperature and low-temperature studies. The galvanostatic charge discharge (GCD) values of the electrodes were recorded in the potential range of 1.5-4.3 V at different specific currents of 0.1, 0.2 0.5, 1, 2, and 5C. The cycling studies were performed with the following C rate (1 C = 136 mA g^{-1}) at various temperatures (0.2 C for RT, and 0.1 C for LT of -20 °C). Similarly, the cyclic voltammetry (CV) profiles were obtained in the same voltage window with varying scan rates of 0.2, 0.4, 0.6, 0.8, and 1 mV s⁻¹. The electrochemical impedance spectroscopy (EIS) measurements were recorded to measure the cell impedance in the range of 1 MHz-0.1 Hz with a voltage perturbation of 0.01 V.

The $\mathrm{Na^+}$ diffusion coefficients $(D_{\mathrm{Na^+}})$ are calculated according to the following equation:

$$D_{\mathrm{Na^{+}}} = \frac{4}{\pi\tau} \left(\frac{m_{\mathrm{B}} V_{\mathrm{M}}}{M_{\mathrm{B}} S} \right)^{2} \left(\frac{\Delta E_{\mathrm{S}}}{\Delta E_{\tau}} \right)^{2}$$

where τ is the time interval for the galvanostatic current applied. $M_{\rm B}$ and $m_{\rm B}$ are the molecular weight and the active material mass, respectively. $V_{\rm m}$ represents the molar volume, and S is the surface area of the electrode. $\Delta E_{\rm S}$ and ΔE_{τ} are the steady-state voltage and the total change of the cell voltage E during the current pulse, respectively.

■ RESULTS AND DISCUSSION

The pristine and LiF-incorporated samples were synthesized using a facile sol—gel process, followed by high-temperature calcination, as described in the Synthesis of NMC and LiF-Incorporated NMC Cathode Materials section. The successful incorporation of lithium was confirmed by the ICP-OES analysis, and the presence of fluorine was determined through energy-dispersive X-ray spectroscopy (EDS). The exact ratio of the metal components in the obtained products is provided in Table S1. For ease of reference, the samples $Na_{0.67}Nm_{0.5}Co_{0.5}O_2$, $Na_{0.67}Li_{0.07}Mn_{0.5}Co_{0.5}O_{2-x}F_x$, and $Na_{0.67}Li_{0.13}Mn_{0.5}Co_{0.5}O_{2-y}F_y$ will be, respectively, marked as NMC, NMC-L1, and NMC-L2. The pristine and LiF-

incorporated NMC samples were subjected to powder X-ray diffraction (PXRD) for phase analysis. The resulting XRD patterns and the corresponding Rietveld analysis are shown in Figure 1. The refined XRD patterns indicate the formation of a P3-type cathode (a = b = 2.826 Å, c = 16.876 Å, space group R3m) for the NMC material. Upon Li integration, the diffraction patterns remain the same, except for the additional peak at 2θ of 18.5° which is designated to the (003) plane of the O3 phase.³⁸ The Rietveld-refined lattice parameters are shown in Table S2 for all the samples. The results indicate that the obtained materials are biphasic in nature. The calculated P3/O3 mass percentages from the Rietveld analysis are ~95/5 and ~91/9 in NMC-L1 and NMC-L2, respectively. 38,39 The mixed P/O cathodes displayed lattice parameters a = b = 2.830Å, c = 16.786 for the P3 component and a = b = 2.855, c =14.2336 for O3 for NMC-L1 and a = b = 2.833, c = 16.718 for the P3 component and a = b = 2.851, c = 14.176 for O3 for NMC-L2. Li ions can either occupy the transition-metal sites or sodium-ion sites. According to the obtained Rietveld-refined results and previous literature, we believe that the majority of Li ions occupy the alkali sites, yielding the O3 phase. 40,41 Recently, Zheng et al. reported enhancement in the O3 phase with Li incorporation into a series of biphasic P2/O3 cathodes.40 However, upon Li integration, the percentage of the O3 phase increased along with a slight positive shift in the (003) plane, indicating a shrinkage in the lattice size owing to the difference in the size of Li and Na ions (see Figure S1). A recent report by Stansby et al. suggests that the O3 phase is stabilized by a high alkali site occupancy. 42 Moreover, the slightly increased O3 percentage with Li incorporation corroborates the presence of Li in the alkali site. Compared to NMC, NMC-L1 and NMC-L2 samples exhibit a reduced lattice parameter 'c' and unit cell volume, further indicating the shrinkage of the unit cell upon LiF addition. This confirms the successful incorporation of Li and F ions into the sodium and oxygen sites of NMC, respectively. The lattice parameters and more detailed analyses are given in Table S2 of the Supporting Information.

The shape and size of the cathode materials were analyzed using TEM and FESEM techniques. The NMC material exhibited agglomerated structures with a nonuniform size of

200–600 nm and hexagonal morphology, with the diagonal length ranging from \sim 0.5 to 3 μ m, and the images are shown in Figure 2. Upon an increase in the O3 phase, for both

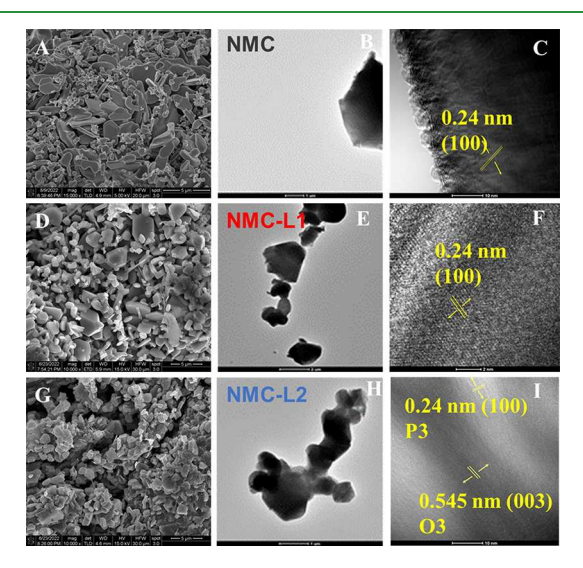


Figure 2. SEM, TEM, and HRTEM analyses of (A-C) NMC, (D-F) NMC-L1, and (G-I) NCM-L2.

samples NMC-L1 and NMC-L2, the hexagonal morphology became more uniform with a very smooth surface, and a slightly increased diagonal length of \sim 0.6–3.5 μ m is noted. The observed morphological features have been reported for a few Li-integrated cathodes which result in an increased contact area of the electrode–electrolyte interface. These features inculcate faster Na⁺ transport kinetics and improve the overall cyclic stability and rate performance. The calculated interlayer spacing value from the HRTEM analysis is $d = \sim$ 0.240 nm, which corresponds to the (100) plane of P3 in all the samples. Additionally, in the biphasic cathodes, lattice fringes with the d-spacing value of 5.45 Å, corresponding to the (003) plane of the O3 phase, were observed (Figure 2I and S2A). Moreover, the EDS mapping confirms the presence of fluorine in the system. The F element composition deduced

from EDS is 0.054 and 0.087 in NMC-L1 and NMC-L2 samples, respectively. Further, the elemental mappings confirm the uniform distribution of sodium, manganese, cobalt, oxygen, and fluorine elements in the corresponding samples (Figures S2 and S3).

The chemical states of the transition metals in the cathode materials were characterized using the XPS analysis (Figures 3 and S4). In the Na 1s spectrum shown in Figure S4, the peak evident at 1070 eV is from Na⁺. Both the pristine and NCM-L1 cathodes display similar peaks of Co 2p and Mn 2p spectra.

The Co 2p spectra given in Figure 3B,D display peaks at 795.1 and 780 eV corresponding to Co $2p_{1/2}$ and Co $2p_{3/2}$, confirming the presence of trivalent cobalt species. 46,47 The Mn 2p spectrum shows two major peaks at 642 and 654 eV attributed to Mn 2P3/2 and Mn 2p1/2, which can be further deconvoluted into four major peaks. The peaks located at 641.7 and 644 eV can be ascribed to Mn3+ and Mn4+, respectively, (Figure 3A,C).⁴⁸ The results are in accordance with the previously reported layered oxide materials. 21,38 Additionally, the tetravalent-to-trivalent manganese ion ratio (Mn⁴⁺:Mn³⁺) is found to be 0.62 and 1.06 in the pristine and NMC-L1 samples. The high-spin Mn³⁺ causes the Jahn-Teller effect which can lead to structural deformation, thus reducing the electrochemical performances. The Li incorporation has led to increased Mn4+ content, which we believe alleviates the Jahn-Teller effect and stabilizes the structures to improve the cyclic stability and rate capability.44

The electrochemical performance of the NMC cathodes is evaluated in a half-cell configuration. The CV curves of the NMC and NMC-L1 samples obtained in the voltage window 1.5–4.3 V at a scan rate of 0.2 mV s⁻¹ are shown in Figure 4A,B. The CV profiles of samples displayed the Mn oxidation and reduction peaks at lower voltage regions of 2 and 1.8 V, respectively.⁴⁹ Further, the sharp oxidation peaks observed at 3.4, 3.7, and 4.02 V and the reduction peaks at 3.34, 3.6, and 3.98 V can be ascribed to the Co³⁺/Co⁴⁺ redox couple.⁵⁰ The peak below the low voltage 2.0 V indicates that Mn⁴⁺ is activated after the Na insertion.⁵¹ In the pristine cathode, the CV curve in the low-voltage region of 2.3–1.9 V shows multiple peaks, which is absent in NMC-L1, and the observed

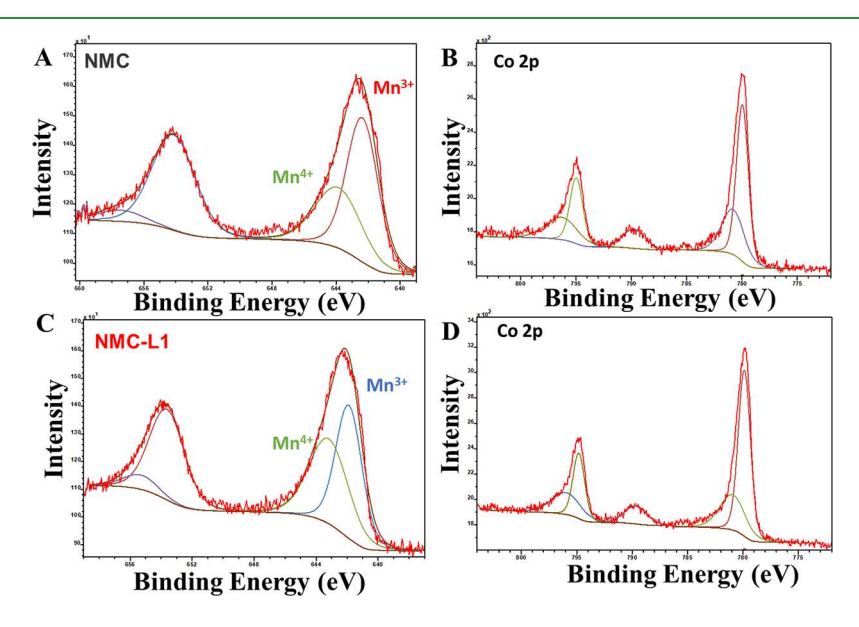


Figure 3. XPS spectra of Mn 2p and Co 2p in (A, B) NMC and (C, D) NMC-L1 cathodes, respectively.

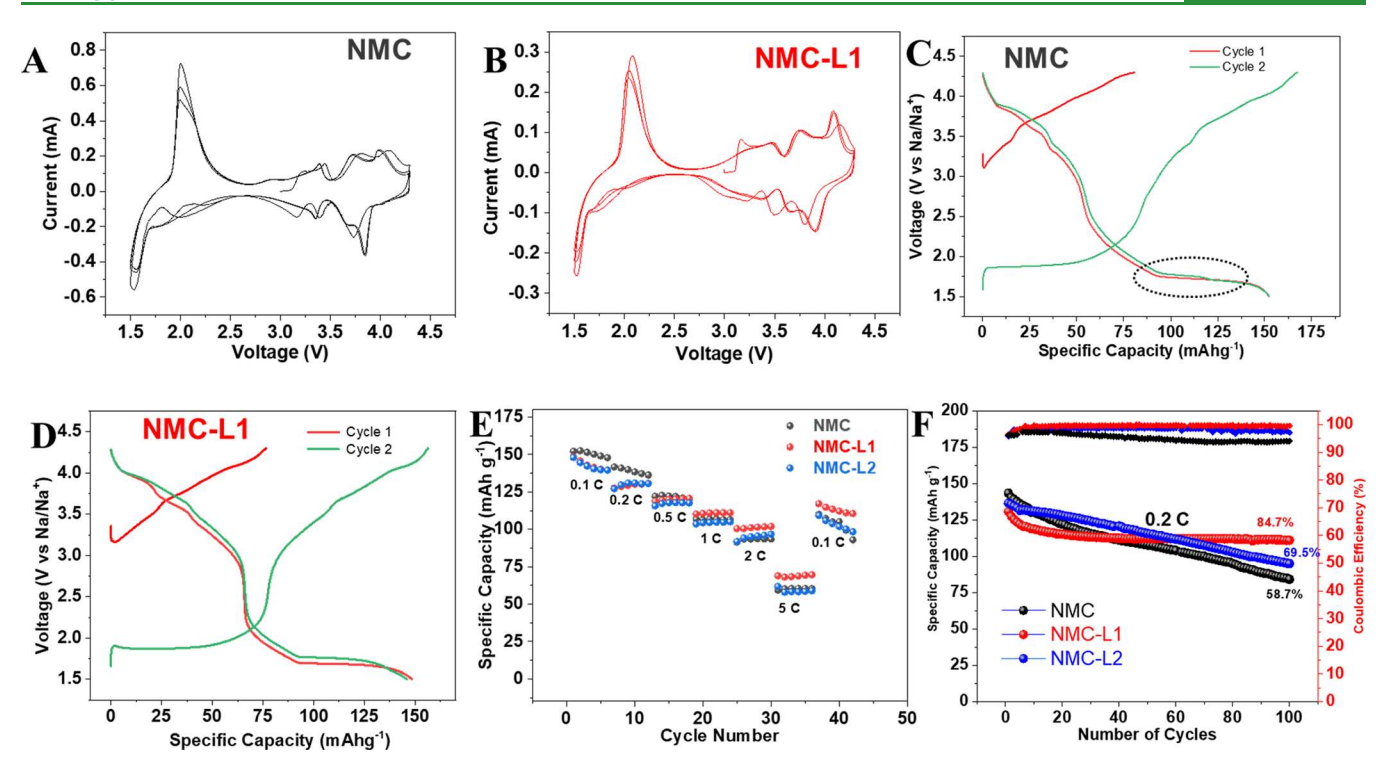


Figure 4. CV curves at 0.2 mV s^{-1} (A, B) and GCD profiles at 0.1 C (C, D) of NMC and NMC-L1, respectively, and (E) rate studies and (F) cyclic stability of cathodes.

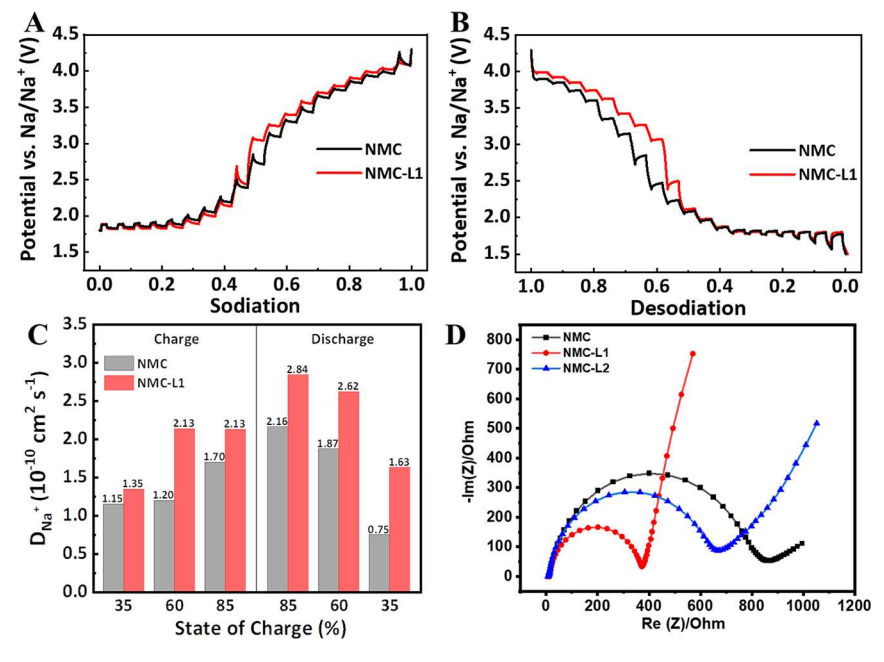


Figure 5. GITT plots for (A) charge and (B) discharge. (C) Diffusion coefficients and (D) EIS.

peaks become sharper, indicating feasible sodiation and desodiation. The consecutive cycles after the first cycle of NMC-L1 displayed barely any change in the peak position, illustrating higher stability and excellent reversibility. The CV and GCD profiles of the NCM-L2 cathode are shown in Figure S5. The galvanostatic charge—discharge curves of the pristine and NCM-L1 cathodes for the first two cycles in the voltage window 1.5–4.3 V are shown in Figure 4C,D, recorded at 0.1 C (1 C = 136 mAh g $^{-1}$). The GCD curves mirror the features observed in the CV profiles. It can be clearly elucidated that

the multiple-phase transformations are suppressed in the NMC-L1 sample during discharge as it possesses only one plateau in the lower voltage region, while the pristine sample has two plateaus. The voltage profiles display two plateaus corresponding to $\mathrm{Co^{3+}/Co^{4+}}$ and $\mathrm{Mn^{4+}/Mn^{3+}}$ redox reactions, respectively. The lower initial charge capacity given in the first cycle was from Na⁺ extraction from the cathode, when charged to 4.3 V, solely to $\mathrm{Co^{3+/4+}}$ oxidation.

The pristine cathode demonstrates a high initial discharge capacity of $152~\text{mAhg}^{-1}$ at a 0.1~C (15 mA g $^{-1}$) rate, with

simultaneous reduction of Mn^{4+/3+} and Co^{4+/3+} in the region 1.5–4.3 V vs Na.⁵² Similarly, slightly reduced capacities of 149 and 148 mAhg⁻¹ are observed in the NMC-L1 and NMC-L2 cathodes, respectively. The slight drop in specific capacity may be attributed to the incorporation of inactive Li⁺ species.⁴² Though there is an initial drop in the capacity value, the overall cyclic stability increased in LiF-incorporated cathodes. It is noted that the NMC-L1 cathode is the optimized cathode due to 85% capacity retention after 100 cycles with a high Coulombic efficiency of 99% at 0.2C rate (Figure 4F), whereas capacity retention of 74 and 58% was obtained for NMC-L2 and pristine cathodes, respectively. Recently, Guo et al. demonstrated a mixed P2-O3 cathode with Li doping for improved capacity retention, cyclic stability, and high energy density.²⁹ The multistep plateau profile in the GCD curves of cathodes is inevitable due to the usage of redox active transition metals. Though, this phenomenon leads to structural changes and capacity fade, the optimized cathode NMC-L1 possesses long cyclic stability and better rate performance, making it a better candidate for general applications.³³

The above results suggest that Li integration greatly enhances the structural stability. Although the pristine cathode possesses a slightly higher initial capacity, the noted larger capacity fade in the pristine cathode can be attributed to the structural instability and Jahn-Teller distortions associated with the Mn3+ ions. Further, the rate capability analysis was performed for the cathodes with different current densities in the 1.5-4.3 V range. The specific capacity values gradually decrease with increasing scan rates due to the limitations of diffusion kinetics of the electrode materials. Further, the rate performance of the cathode was evaluated at different C rates, and the results are shown in Figure 4E. The pristine NMC cathode reveals a specific capacitance of 152, 141, 122, 107, 91, and 59 mAh g⁻¹ at 0.1 (15), 0.2 (30), 0.5 (75), 1 (150), 2 (300), and 5C (750 mA g^{-1}). The NMC-L1 samples delivered 149, 129, 119, 110, 101, and 69 mAh g⁻¹, whereas the NMC-L2 displayed 148, 127, 116, 104, 92, and 58 mAh g⁻¹ capacitances at 0.1 (15), 0.2 (30), 0. 5(75), 1 (150), 2 (300), and 5C (750 mA g⁻¹) rates. At higher specific currents (0.5-5C), the biphasic cathode NMC-L1 displays higher specific capacities. These results clearly indicate that the optimized LiF incorporation in pristine NMC cathode enhances the rate capability at higher current densities.

The Na $^+$ transportation kinetics of the cathodes were evaluated at an equilibrium state using the galvanostatic intermittent titration technique (GITT), as shown in Figure 5A,B. ^{53,54} The cells were charged at 0.1 C rate for 10 min and then allowed to be relaxed for 30 min for attaining an equilibrium voltage. The experimental parameters and other details are given in the Supporting Information. The calculated diffusion coefficient ($D_{\rm Na}^+$) values are in the range of 10^{-10} to 10^{-11} for both P3(NMC) and P3/O3 (NMC-L1) cathodes.

The $D_{\rm Na^+}$ values are slightly higher for the NMC-L1 sample $(1.35-2.13\times 10^{-10}~{\rm cm^2~s^{-1}}$ during charge and $2.84-1.63\times 10^{-10}~{\rm cm^2~s^{-1}}$ in discharge) compared to the pristine NMC cathode $(1.15-1.70\times 10^{-10}~{\rm cm^2~s^{-1}}$ during charge and $2.16-0.75\times 10^{-10}~{\rm cm^2~s^{-1}}$ in discharge) during sodiation and desodiation processes (Figure 5C). A higher $D_{\rm Na^+}$ value indicates faster sodium diffusion kinetics, leading to a better rate capability in the NMC-L1 cathode. During the discharge process, there was a reduction in the $D_{\rm Na^+}$ values in both samples, indicating that the sluggish Na⁺ diffusion can be ascribed to the Jahn–Teller effect and increased Na⁺–Na⁺

electrochemical interactions. ⁵⁵ However, it can be clearly noted that the rapid dip in the $D_{\rm Na^+}$ value of the pristine sample is due to sluggish kinetics and the Jahn–Teller distortions, which are alleviated in the case of LiF-integrated NMC-L1 cathode.

The CV curves of the as-synthesized cathodes obtained at different scan rates from 0.2 to 1 mV s⁻¹ show increased peak currents (Figure S6). The Na+ kinetics is further analyzed using the Randles-Sevcik equation $i = av^b (\log (i) = b\log (v) +$ $\log(a)$, where i is the current, v is the scan rate, and a and b are empirical parameters, respectively). A b value closer to 1 represents a surface capacitance process, whereas a b value of 0.5 indicates a diffusion-controlled process. To evaluate the bvalue, the CV curves of the half-cells were recorded at varying scan rates, and logarithmic plots were constructed by plotting the scan rate versus current. The obtained averaged b values for different peaks are 0.85 and 0.93 for NMC and NMC-L1 samples, respectively. The obtained values are closer to 1, suggesting a higher capacitance contribution involving rapid Na+ diffusion kinetics. Furthermore, the mechanism can be distinguished from a surface-controlled or Faradaic intercalation from the following equations 56,5

$$i = k_1 \nu + k_2 \nu^{1/2}$$

 $i/\nu^{1/2} = k_1 \nu^{1/2} + k_2$

where k_1 and k_2 are constants, the $k_1 \nu$ component is the capacitance contribution, and $k_2 \nu^{1/2}$ represents the diffusioncontrolled mechanism. Figure S6 represents the bar diagram distinguishing the pseudocapacitance and diffusion contributions with varying scan rates. For the NMC-L1 cathode, even at the lower scan rate of 0.2 mV s⁻¹, the capacitance contribution is very high, 75%. On further increasing the scan rate to 1 mV s⁻¹, the capacitance contribution increases to 87%, indicating the faster sodium transfer kinetics. The diffusion of Na+ into the bulk is the major bottleneck for most of the conventional sodium cathodes, thereby leading to poor rate performance. In the case of the NMC-L1 cathode, the observed dominant surface capacitance enables shorter diffusion paths resulting in facilitated sodiation and desodiation. Additionally, the EIS studies performed in the frequency range between 0.1 Hz and 100 kHz illustrate the lower impedance for the NMC-L1 sample compared to Li-free P3-NMC with a lower charge-transfer resistance, indicating better Na⁺ diffusion kinetics (Figure 5D). In the Nyquist plots, the radius of the semicircle can be considered as the chargetransfer resistance (R_{ct}), and the R_{ct} values are determined as 825, 380, and 620 Ohms for NMC, NMC-L1, and NMC-L2 cathodes, respectively, indicating higher conductivity in LiFincorporated cathodes. Warburg impedance that appears as a diagonal line in the Nyquist plot represents the diffusion behavior, and from Figure 5D, the improved Warburg impedance can be observed in the sample NMC-L1. These results suggest that LiF integration can promote the Na+ kinetics in the biphasic cathode and consequently improve the electrochemical properties of the cathodes.

Additionally, the excellent structural stabilization by LiF incorporation in the NMC-L1 cathode is further corroborated by the coexistence of P3/O3 phases after 100 cycles at 0.1 C using ex situ X-ray diffraction analysis, Figure S7. The LiF integration helps in improving the morphological features for better electrolyte–electrode interactions. The Jahn–Teller effect has been alleviated to some extent by Li incorporation.

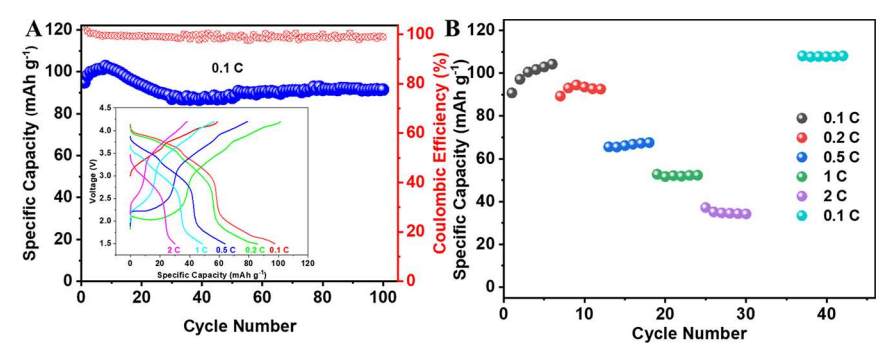


Figure 6. Subzero temperature (-20 °C) performance of the optimized NMC-L1 cathode. (A) Cyclic stability with Coulombic efficiency at 0.1 C; inset shows GCD profiles at different C rates. (B) Rate studies.

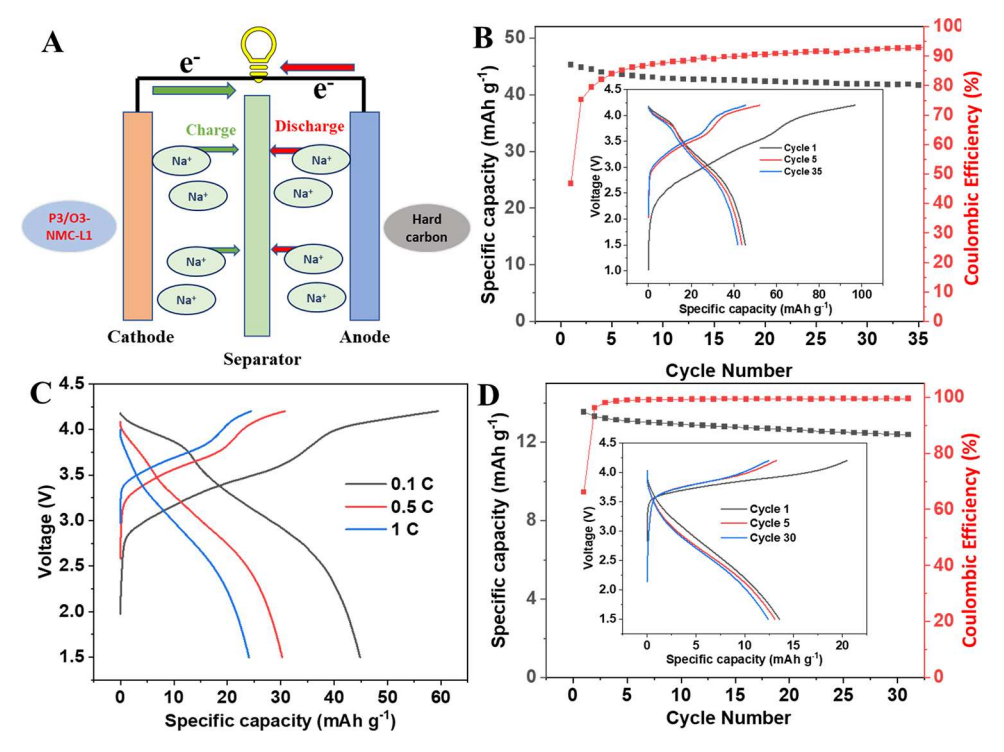


Figure 7. (A) Schematic of the full cell, (B) cyclic stability at 25 °C (inset: GCD at different cycles), (C) GCD curves at different C rates, and (D) cyclic stability at -20 °C.

Besides the Jahn-Teller effect, the layered oxide cathodes suffer from capacity fading and voltage drop at high charging voltages as the lattice oxygen escapes due to the anionic redox reaction.⁵⁸ The F ion aided in stronger TM-O(F) bonds, which resulted in the structural stabilization of the cathodes. In this regard, replacement of O²⁻ ions with F⁻ ions is found to improve the cycle life of both Li- and Na-ion batteries. 59 The incorporation of more electronegative F- ions results in the formation of stronger TM-F bond which significantly reduces the electrostatic repulsion between the oxygen layers.³² Consequently, the gliding of TMO2 layers can be restricted such that the layered oxide cathodes could achieve improved structural stability and cyclic performance even at high charging voltages. The cathode with 7% Li incorporation displayed excellent Na storage ability with improved cyclic stability and rate performance. However, with an increase in the Li concentration to 13% in NMC-L2, there is a reduction in capacity value, though it displayed good stability. The noted slightly declined performance relative to the NCM-L1 sample may be attributed to the increased O3 phase and the relatively

higher charge-transfer resistance, as evident from the EIS studies.⁶⁰

Low-Temperature Performance. The majority of the stable P-type, O-type, or biphasic cathodes are well studied for SIBs at room temperatures, but there are few reports on low-temperature applications.⁶¹ Additionally, after 200 cycles of charge—discharge at 0.2 C (30 mA g⁻¹) for the cathodes at room temperature, a capacity retention of 73.18% is observed for NMC-L1, which is far superior to that of NMC (27.53%), as shown in Figure S8A. Further, at subzero temperature, the cyclic stability of NMC-L1 was better than that of pristine cathode at 0.5 C (75 mA g⁻¹) rate (Figure S8B).

Hence, we studied the best-performing P3/O3 NMC-L1 cathode and evaluated its performance at a subzero temperature of -20 °C. The GCD curves of the cathode are presented in the inset of Figure 6A, and the specific capacity values are found to be 97, 85, 63, 48, and 32 mAhg⁻¹ at C rates of 0.1 (15), 0.2 (30), 0.5 (75), 1 (150), and 2 (300 mA g⁻¹), respectively. The capacity value at 0.1 C (15 mA g⁻¹) is ~65% of that of the room-temperature value, and the observed

capacity retention values are comparable to few layered oxide cathodes reported previously (Figure S8C and Table S3). Further, the cathode possesses superior long-term cycling stability, as shown in Figure 6A, even after 100 cycles at 0.1 C (15 mA g⁻¹), with excellent retention, of 94% of the initial capacity and nearly 99% Coulombic efficiency. Additionally, the rate studies were examined at various current rates, and the cathode delivered reversible discharge capacities, elucidating better rate capability than that at room temperature, as depicted in Figure 6B.

Further, a full cell was constructed to check the extreme temperature performance with an optimized NMC-L1 cathode and a hard carbon anode (without presodiation for practical applications) using 1 M NaPF₆ in PC as the electrolyte, as shown in Figure 7A.⁶² Prior to the full cell assembly, the hard carbon Na-ion storage properties are measured at room temperature at $20~\text{mA}~\text{g}^{-1}$ current density, showing a capacity of 183 mAh g⁻¹ in the second discharge cycle (Figure S9). It is noted that the full cell delivered an initial discharge capacity of 45 mAh g⁻¹ (specific energy of 151.48 Wh kg⁻¹), with \sim 94% retention after 35 cycles at room temperature, calculated based on the cathode mass, as shown in Figure 7B. The full cell capacity was recorded at different current rates, 0.5 C (75 mA g⁻¹) and 1 C (150 mA g⁻¹), where discharge capacities of 30.26 mAh g^{-1} and 24.02 mAh g^{-1} are obtained (Figure 7C). Further, the NMC-L1||HC full cell was operated at a subzero temperature of -20 °C. The full cell delivered an initial capacity of 13.54 mAh g⁻¹ at 0.1 C (15 mA g⁻¹) rate with the capacity retention of 92% after 30 cycles and excellent Coulombic efficiency of 99.5%, as depicted in Figure 7D.

Additionally, the full cell performance was recorded at 0.1 C (15 mA g⁻¹) at various temperatures ranging from -20 to +50 $^{\circ}$ C, and excellent capacity retention was noted at different temperatures (Figure S10). The initial capacity was regained during the transition from low temperature ($-20~^{\circ}$ C) to room temperature (25 $^{\circ}$ C). At a high temperature (50 $^{\circ}$ C), the capacity slightly improved with very good cycling stability, demonstrating excellent cyclic stabilities of the full cell at a wider temperature range of -20 to 50 $^{\circ}$ C.

CONCLUSIONS

To summarize, a stable P3/O3 biphasic sodium-layered oxide cathode was developed through a facile LiF incorporation strategy for applications at low temperatures. The optimized cathode displayed excellent sodium storage capabilities at both room temperature and subzero temperatures. It delivered an initial capacity of 148 mAh g⁻¹ at 0.1 C (15 mA g⁻¹) and good cyclic stability with 85% retention in capacity at 0.2 C (30 mA g^{-1}) rate after 100 cycles within a potential window of 1.5–4.3 V. The incorporation of LiF improved the performance by alleviating the Jahn-Teller effect through Li, and the presence of fluorine atoms resulted in more stable TM-O(F) bonds. The cathode material displayed excellent structural stability with a well-matched crystal structure after cyclic stability. Majority of the layered oxide cathodes or their composites are reported for SIB applications at room temperature but seldom studied at low temperatures. Even at low temperatures, the capacity retention was 94% of the initial capacity. Further, a full cell comprising a hard carbon anode and a biphasic cathode with 1 M NaPF₆ electrolyte displayed excellent cyclic stabilities at a wider temperature range of -20 to 50 °C (with the energy density of 151.48 Wh kg⁻¹) due to enhanced structural stability, alleviated Jahn-Teller distortions, and

rapid Na⁺ kinetics facilitating Na⁺ motion at various temperatures in SIBs. This strategy to engineer multiphasic cathodes will enable the exploration of new materials to push the boarders toward ultralow-temperature SIB applications.

ASSOCIATED CONTENT

Supporting Information

The Supporting Information is available free of charge at https://pubs.acs.org/doi/10.1021/acsami.3c03386.

Electrochemical studies; cyclic stability studies; full-cell and half-cell studies; postcharacterization studies; ICP-OES data; Rietveld refinement parameters; SEM, TEM, and EDS analyses; charge storage mechanism; and comparison of electrochemical activities (PDF)

AUTHOR INFORMATION

Corresponding Author

Vilas G. Pol — Davidson School of Chemical Engineering, Purdue University, West Lafayette, Indiana 47907, United States; ⊚ orcid.org/0000-0002-4866-117X; Email: vpol@ purdue.edu

Authors

Heramba Venkata Sai Rama Murthy Koppisetti — Davidson School of Chemical Engineering, Purdue University, West Lafayette, Indiana 47907, United States; Department of Chemical Sciences, Indian Institute of Science Education and Research (IISER), 741246 Nadia, West Bengal, India

Harsha Rao – Davidson School of Chemical Engineering, Purdue University, West Lafayette, Indiana 47907, United States

Hari Vignesh Ramasamy — Davidson School of Chemical Engineering, Purdue University, West Lafayette, Indiana 47907, United States; orcid.org/0000-0002-8241-2441

Harish Reddy Inta — Department of Chemical Sciences, Indian
Institute of Science Education and Research (IISER), 741246
Nadia, West Bengal, India

Sayan Das − Davidson School of Chemical Engineering, Purdue University, West Lafayette, Indiana 47907, United States; orcid.org/0000-0002-4730-7312

Soohwan Kim — Davidson School of Chemical Engineering, Purdue University, West Lafayette, Indiana 47907, United States; orcid.org/0000-0003-1290-5539

Yizhi Zhang — School of Materials Engineering, Purdue University, West Lafayette, Indiana 47907, United States Haiyan Wang — School of Materials Engineering, Purdue University, West Lafayette, Indiana 47907, United States; orcid.org/0000-0002-7397-1209

Venkataramanan Mahalingam — Department of Chemical Sciences, Indian Institute of Science Education and Research (IISER), 741246 Nadia, West Bengal, India; © orcid.org/0000-0003-1414-805X

Complete contact information is available at: https://pubs.acs.org/10.1021/acsami.3c03386

Author Contributions

The manuscript was written through contributions of all authors. All the images/artwork/photos that appear in the manuscript and Supporting Information, including those in the TOC graphic, were created by the authors of this study.

Notes

The authors declare no competing financial interest.

ACKNOWLEDGMENTS

The authors thank Purdue University's 'Trask Innovation Funds' for the financial support. Y.Z. and H.W. acknowledge the support from the U.S. National Science Foundation (DMR-2016453 and DMR-1809520) for the TEM effort at Purdue University. H.V.S.R.M.K. thanks SERB India for his fellowship. The authors thank Dr. Manjusha, Zheng, Daniel, Ethan, Arya, and Soohwan for their constructive suggestions to structure this work. They thank Dr. Kingshuk for help with MATLAB programming. The authors acknowledge Dr. Dimitry Zemlyanov for XPS measurements at Birck Nanotechnology Center, Purdue University.

REFERENCES

- (1) Miocic, J. M.; Alcalde, J.; Heinemann, N.; Marzan, I.; Hangx, S. Toward Energy-Independence and Net-Zero: The Inevitability of Subsurface Storage in Europe. ACS Energy Lett. 2022, 7, 2486–2489.
- (2) Luo, B.; Ye, D.; Wang, L.; Luo, B.; Ye, D.; Wang, L. Recent Progress on Integrated Energy Conversion and Storage Systems. *Adv. Sci.* **2017**, *4*, No. 1700104.
- (3) Armand, M.; Tarascon, J. M. Building Better Batteries. *Nature* **2008**, *451*, 652–657.
- (4) Slater, M. D.; Kim, D.; Lee, E.; Johnson, C. S. Sodium-Ion Batteries. *Adv. Funct. Mater.* **2013**, 23, 947–958.
- (5) Alvira, D.; Antorán, D.; Manyà, J. J. Plant-Derived Hard Carbon as Anode for Sodium-Ion Batteries: A Comprehensive Review to Guide Interdisciplinary Research. *Chem. Eng. J.* **2022**, 447, No. 137468.
- (6) Mukai, K.; Inoue, T.; Kato, Y.; Shirai, S. Superior Low-Temperature Power and Cycle Performances of Na-Ion Battery over Li-Ion Battery. ACS Omega 2017, 2, 864–872.
- (7) Soda Ash in Mineral Commodity Summaries 2022; U.S. Geological Survey: Reston, VA, 2022; p 155.
- (8) Peters, J. F.; Baumann, M.; Binder, J. R.; Weil, M. On the Environmental Competitiveness of Sodium-Ion Batteries under a Full Life Cycle Perspective a Cell-Chemistry Specific Modelling Approach. Sustainable Energy Fuels 2021, 5, 6414—6429.
- (9) Kundu, D.; Talaie, E.; Duffort, V.; Nazar, L. F. The Emerging Chemistry of Sodium Ion Batteries for Electrochemical Energy Storage. *Angew. Chem., Int. Ed.* **2015**, *54*, 3431–3448.
- (10) Hwang, J. Y.; Myung, S. T.; Sun, Y. K. Sodium-Ion Batteries: Present and Future. Chem. Soc. Rev. 2017, 46, 3529-3614.
- (11) You, Y.; Manthiram, A. Progress in High-Voltage Cathode Materials for Rechargeable Sodium-Ion Batteries. *Adv. Energy Mater.* **2018**, *8*, No. 1701785.
- (12) Liu, T.; Zhang, Y.; Jiang, Z.; Zeng, X.; Ji, J.; Li, Z.; Gao, X.; Sun, M.; Lin, Z.; Ling, M.; Zheng, J.; Liang, C. Exploring Competitive Features of Stationary Sodium Ion Batteries for Electrochemical Energy Storage. *Energy Environ. Sci.* **2019**, *12*, 1512–1533.
- (13) Niu, Y.-B.; Yin, Y.-X.; Guo, Y.-G. Nonaqueous Sodium-Ion Full Cells: Status, Strategies, and Prospects. *Small* **2019**, *15*, No. 1900233.
- (14) Li, Y.; Lu, Y.; Adelhelm, P.; Titirici, M. M.; Hu, Y. S. Intercalation Chemistry of Graphite: Alkali Metal Ions and Beyond. *Chem. Soc. Rev.* **2019**, *48*, 4655–4687.
- (15) Han, M. H.; Gonzalo, E.; Singh, G.; Rojo, T. A Comprehensive Review of Sodium Layered Oxides: Powerful Cathodes for Na-Ion Batteries. *Energy Environ. Sci.* **2014**, *8*, 81–102.
- (16) Delmas, C.; Fouassier, C.; Hagenmuller, P. Structural Classification and Properties of the Layered Oxides. *Physica B+C* **1980**, 99, 81–85.
- (17) Wang, P.-F.; You, Y.; Yin, Y.-X.; Guo, Y.-G. Layered Oxide Cathodes for Sodium-Ion Batteries: Phase Transition, Air Stability, and Performance. *Adv. Energy Mater.* **2018**, *8*, No. 1701912.
- (18) Wang, J. E.; Kim, H.; Jung, Y. H.; Kim, D. K.; Kim, D. J. Designing High Energy Sodium-Ion Battery Cathodes by Utilizing P2/O3 Biphasic Structure and Lithium Honeycomb Ordering. *Small* **2021**, *17*, No. 2100146.

- (19) Lei, Y.; Li, X.; Liu, L.; Ceder, G. Synthesis and Stoichiometry of Different Layered Sodium Cobalt Oxides. *Chem. Mater.* **2014**, *26*, 5288–5296.
- (20) Gao, R. M.; Zheng, Z. J.; Wang, P. F.; Wang, C. Y.; Ye, H.; Cao, F. F. Recent Advances and Prospects of Layered Transition Metal Oxide Cathodes for Sodium-Ion Batteries. *Energy Storage Mater.* **2020**, *30*, 9–26.
- (21) Ramasamy, H. V.; Kaliyappan, K.; Thangavel, R.; Seong, W. M.; Kang, K.; Chen, Z.; Lee, Y. S. Efficient Method of Designing Stable Layered Cathode Material for Sodium Ion Batteries Using Aluminum Doping. *J. Phys. Chem. Lett.* **2017**, *8*, 5021–5030.
- (22) Zhou, P.; Che, Z.; Liu, J.; Zhou, J.; Wu, X.; Weng, J.; Zhao, J.; Cao, H.; Zhou, J.; Cheng, F. High-Entropy P2/O3 Biphasic Cathode Materials for Wide-Temperature Rechargeable Sodium-Ion Batteries. *Energy Storage Mater.* **2023**, *57*, 618–627.
- (23) Feng, J.; Fang, D.; Yang, Z.; Zhong, J.; Zheng, C.; Wei, Z.; Li, J. A Novel P2/O3 Composite Cathode toward Synergistic Electrochemical Optimization for Sodium Ion Batteries. *J. Power Sources* **2023**, 553, 232292–232292.
- (24) Hemalatha, K.; Jayakumar, M.; Bera, P.; Prakash, A. S. Improved Electrochemical Performance of Na0.67MnO2 through Ni and Mg Substitution. *J. Mater. Chem. A* **2015**, 3, 20908–20912.
- (25) Fang, C.; Huang, Y.; Zhang, W.; Han, J.; Deng, Z.; Cao, Y.; Yang, H. Routes to High Energy Cathodes of Sodium-Ion Batteries. *Adv. Energy Mater.* **2016**, *6*, No. 1501727.
- (26) Xiao, Y.; Mahmood Abbasi, N.; Zhu, Y.-F.; Li, S.; Tan, S.-J.; Ling, W.; Peng, L.; Yang, T.; Wang, L.; Guo, X.-D.; Yin, Y.-X.; Zhang, H.; Guo, Y.-G. Layered Oxide Cathodes Promoted by Structure Modulation Technology for Sodium-Ion Batteries. *Adv. Funct. Mater.* **2020**, *30*, No. 2001334.
- (27) Yabuuchi, N.; Kubota, K.; Dahbi, M.; Komaba, S. Research Development on Sodium-Ion Batteries. *Chem. Rev.* **2014**, *114*, 11636–11682.
- (28) Wang, K.; Wu, Z. G.; Melinte, G.; Yang, Z. G.; Sarkar, A.; Hua, W.; Mu, X.; Yin, Z. W.; Li, J. T.; Guo, X. D.; Zhong, B. H.; Kübel, C. Preparation of Intergrown P/O-Type Biphasic Layered Oxides as High-Performance Cathodes for Sodium Ion Batteries. *J. Mater. Chem. A* **2021**, *9*, 13151–13160.
- (29) Guo, S.; Liu, P.; Yu, H.; Zhu, Y.; Chen, M.; Ishida, M.; Zhou, H. A Layered P2- and O3-Type Composite as a High-Energy Cathode for Rechargeable Sodium-Ion Batteries. *Angew. Chem., Int. Ed.* **2015**, 54, 5894–5899.
- (30) De La Llave, E.; Talaie, E.; Levi, E.; Nayak, P. K.; Dixit, M.; Rao, P. T.; Hartmann, P.; Chesneau, F.; Major, D. T.; Greenstein, M.; Aurbach, D.; Nazar, L. F. Improving Energy Density and Structural Stability of Manganese Oxide Cathodes for Na-Ion Batteries by Structural Lithium Substitution. *Chem. Mater.* **2016**, *28*, 9064–9076.
- (31) Li, L.; Su, G.; Lu, C.; Ma, X.; Ma, L.; Wang, H.; Cao, Z. Effect of Lithium Doping in P2-Type Layered Oxide Cathodes on the Electrochemical Performances of Sodium-Ion Batteries. *Chem. Eng. J.* **2022**, *446*, No. 136923.
- (32) Liu, Z.; Zhou, C.; Liu, J.; Yang, L.; Liu, J.; Zhu, M. Phase Tuning of P2/O3-Type Layered Oxide Cathode for Sodium Ion Batteries via a Simple Li/F Co-Doping Route. *Chem. Eng. J.* **2022**, 431, No. 134273.
- (33) Ganesan, B. K.; Lee, Y.-S. Phase Transition Induced Enhanced Performance of Sodium-Rich $Na_{1.2}Mn_{0.8}O_{2-y}F_y$ (Y = 0-0.5) Cathodes. ACS Appl. Energy Mater. **2023**, *6*, 960-968.
- (34) Ganesan, B. K.; Moorthy, M.; Thangavel, R.; Nam, K.-W.; Aravindan, V.; Lee, Y.-S. Fluorine Substitution Enabled Superior Performance of $Na_xMn_{2-X}O_{1.5}F_{0.5}$ (X=1.05-1.3) Type Na-Rich Cathode. *Chem. Eng. J.* **2023**, *454*, 139876–139876.
- (35) Wang, C.; Thenuwara, A. C.; Luo, J.; Shetty, P. P.; McDowell, M. T.; Zhu, H.; Posada-Pérez, S.; Xiong, H.; Hautier, G.; Li, W. Extending the Low-Temperature Operation of Sodium Metal Batteries Combining Linear and Cyclic Ether-Based Electrolyte Solutions. *Nat. Commun.* **2022**, *13*, 4934.
- (36) Wang, X.; Yin, X.; Feng, X.; Li, Y.; Dong, X.; Shi, Q.; Zhao, Y.; Zhang, J. Rational Design of Na_{0.67}Ni_{0.2}Co_{0.2}Mn_{0.6}O₂ Microsphere

- Cathode Material for Stable and Low Temperature Sodium Ion Storage. Chem. Eng. J. 2022, 428, No. 130990.
- (37) Yang, Q.; Wang, P. F.; Guo, J. Z.; Chen, Z. M.; Pang, W. L.; Huang, K. C.; Guo, Y. G.; Wu, X. L.; Zhang, J. P. Advanced P2-Na_{2/3}Ni_{1/3}Mn_{7/12}Fe_{1/12}O₂ Cathode Material with Suppressed P2-O2 Phase Transition toward High-Performance Sodium-Ion Battery. *ACS Appl. Mater. Interfaces* **2018**, *10*, 34272–34282.
- (38) Zhang, S.-Y.; Guo, Y.-J.; Zhou, Y.-N.; Zhang, X.-D.; Niu, Y.-B.; Wang, E.-H.; Huang, L.-B.; An, P.-F.; Zhang, J.; Yang, X.-A.; Yin, Y.-X.; Xu, S.; Guo, Y.-G. P3/O3 Integrated Layered Oxide as High-Power and Long-Life Cathode toward Na-Ion Batteries. *Small* **2021**, *17*, No. 2007236.
- (39) Lee, E.; Lu, J.; Ren, Y.; Luo, X.; Zhang, X.; Wen, J.; Miller, D.; DeWahl, A.; Hackney, S.; Key, B.; Kim, D.; Slater, M. D.; Johnson, C. S. Layered P2/O3 Intergrowth Cathode: Toward High Power Na-Ion Batteries. *Adv. Energy Mater.* **2014**, *4*, No. 1400458.
- (40) Li, Z. Y.; Zhang, J.; Gao, R.; Zhang, H.; Zheng, L.; Hu, Z.; Liu, X. Li-Substituted Co-Free Layered P2/O3 Biphasic Na_{0.67}Mn_{0.55}Ni_{0.25}Ti_{0.2-X}Li_xO₂ as High-Rate-Capability Cathode Materials for Sodium Ion Batteries. *J. Phys. Chem. C* **2016**, *120*, 9007–9016.
- (41) Lu, X.; Wang, Y.; Liu, P.; Gu, L.; Hu, Y. S.; Li, H.; Demopoulos, G. P.; Chen, L. Direct Imaging of Layered O3- and P2-Na $_x$ Fe $_{1/2}$ Mn $_{1/2}$ O $_2$ Structures at the Atomic Scale. *Phys. Chem. Chem. Phys.* **2014**, *16*, 21946–21952.
- (42) Stansby, J. H.; Avdeev, M.; Brand, H. E. A.; Gonzalo, E.; Drewett, N. E.; Ortiz-Vitoriano, N.; Sharma, N.; Rojo, T. Biphasic P2/O3-Na_{2/3}Li_{0.18}Mn_{0.8}Fe_{0.2}O₂: A Structural Investigation. *Dalton Trans.* **2021**, *50*, 1357–1365.
- (43) Xiao, Y.; Zhu, Y.-F.; Yao, H.-R.; Wang, P.-F.; Zhang, X.-D.; Li, H.; Yang, X.; Gu, L.; Li, Y.-C.; Wang, T.; Yin, Y.-X.; Guo, X.-D.; Zhong, B.-H.; Guo, Y.-G. A Stable Layered Oxide Cathode Material for High-Performance Sodium-Ion Battery. *Adv. Energy Mater.* **2019**, 9, No. 1803978.
- (44) Liu, Y.; Wang, C.; Zhao, S.; Zhang, L.; Zhang, K.; Li, F.; Chen, J. Mitigation of Jahn—Teller Distortion and Na⁺/Vacancy Ordering in a Distorted Manganese Oxide Cathode Material by Li Substitution. *Chem. Sci.* **2021**, *12*, 1062–1067.
- (45) Ramesh, A.; Tripathi, A.; Bosman, M.; Xi, S.; Balaya, P. Enhancement in Rate Performance and High Voltage Structural Stability of P3/O3 Na_{0.9}Fe_{0.5}Mn_{0.45}Ni_{0.05}O₂ Layered Oxide Cathode. *J. Electroanal. Chem.* **2023**, 932, 117222–117222.
- (46) Dahéron, L.; Dedryvère, R.; Martinez, H.; Ménétrier, M.; Denage, C.; Delmas, C.; Gonbeau, D. Electron Transfer Mechanisms upon Lithium Deintercalation from LiCoO₂ to CoO₂ Investigated by XPS. *Chem. Mater.* **2008**, *20*, 583–590.
- (47) Ghosh, S.; Mondal, A.; Tudu, G.; Ghosh, S.; Koppisetti, H. V. S. R. M.; Inta, H. R.; Saha, D.; Mahalingam, V. Efficient Electrochemical Reconstruction of a Cobalt- and Silver-Based Precatalytic Oxalate Framework for Boosting the Alkaline Water Oxidation Performance. ACS Sustainable Chem. Eng. 2022, 10, 7265—7276.
- (48) Chen, T. R.; Sheng, T.; Wu, Z. G.; Li, J. T.; Wang, E. H.; Wu, C. J.; Li, H. T.; Guo, X. D.; Zhong, B. H.; Huang, L.; Sun, S. G. Cu²⁺ Dual-Doped Layer-Tunnel Hybrid Na_{0.6}Mn_{1-X}Cu_xO₂ as a Cathode of Sodium-Ion Battery with Enhanced Structure Stability, Electrochemical Property, and Air Stability. *ACS Appl. Mater. Interfaces* **2018**, *10*, 10147–10156.
- (49) Shi, Y.; Zhang, Z.; Jiang, P.; Gao, A.; Li, K.; Zhang, Q.; Sun, Y.; Lu, X.; Cao, D.; Lu, X. Unlocking the Potential of P3 Structure for Practical Sodium-Ion Batteries by Fabricating Zero Strain Framework for Na⁺ Intercalation. *Energy Storage Mater.* **2021**, *37*, 354–362.
- (50) Hemalatha, K.; Jayakumar, M.; Prakash, A. S. Influence of the Manganese and Cobalt Content on the Electrochemical Performance of P2-Na_{0.67}Mn_xCo₁–O₂ Cathodes for Sodium-Ion Batteries. *Dalton Trans.* **2018**, 47, 1223–1232.
- (51) Li, Z. Y.; Gao, R.; Sun, L.; Hu, Z.; Liu, X. Designing an Advanced $P2-Na_{0.67}Mn_{0.65}Ni_{0.2}Co_{0.15}O_2$ Layered Cathode Material for Na-Ion Batteries. *J. Mater. Chem. A* **2015**, 3, 16272–16278.

- (52) Ramasamy, H. V.; Didwal, P. N.; Sinha, S.; Aravindan, V.; Heo, J.; Park, C.-J.; Lee, Y.-S. Atomic Layer Deposition of Al₂O₃ on P2-Na_{0.5}Mn_{0.5}Co_{0.5}O₂ as Interfacial Layer for High Power Sodium-Ion Batteries. *J. Colloid Interface Sci.* **2020**, 564, 467–477.
- (53) Shi, Y.; Li, S.; Gao, A.; Zheng, J.; Zhang, Q.; Lu, X.; Gu, L.; Cao, D. Probing the Structural Transition Kinetics and Charge Compensation of the P2-Na_{0.78}Al_{0.05}Ni_{0.33}Mn_{0.60}O₂ Cathode for Sodium Ion Batteries. *ACS Appl. Mater. Interfaces* **2019**, *11*, 24122–24131.
- (54) Kim, S.; Seo, B.; Ramasamy, H. V.; Shang, Z.; Wang, H.; Savoie, B. M.; Pol, V. G. Ion-Solvent Interplay in Concentrated Electrolytes Enables Subzero Temperature Li-Ion Battery Operations. *ACS Appl. Mater. Interfaces* **2022**, *14*, 41934–41944.
- (55) Zuo, W.; Liu, X.; Qiu, J.; Zhang, D.; Xiao, Z.; Xie, J.; Ren, F.; Wang, J.; Li, Y.; Ortiz, G. F.; Wen, W.; Wu, S.; Wang, M. S.; Fu, R.; Yang, Y. Engineering Na⁺-Layer Spacings to Stabilize Mn-Based Layered Cathodes for Sodium-Ion Batteries. *Nat. Commun.* **2021**, *12*, 4903.
- (56) Wang, J.; Polleux, J.; Lim, J.; Dunn, B. Pseudocapacitive Contributions to Electrochemical Energy Storage in TiO₂ (Anatase) Nanoparticles. *J. Phys. Chem. C* **2007**, *111*, 14925–14931.
- (57) Conway, B. E.; Birss, V.; Wojtowicz, J. The Role and Utilization of Pseudocapacitance for Energy Storage by Supercapacitors. *J. Power Sources* **1997**, *66*, 1–14.
- (58) Li, X.-L.; Wang, T.; Yuan, Y.; Yue, X.-Y.; Wang, Q.-C.; Wang, J.-Y.; Zhong, J.; Lin, R.; Yao, Y.; Wu, X.-J.; Yu, X.; Fu, Z.-W.; Xia, Y.; Yang, X.-Q.; Liu, T.; Amine, K.; Shadike, Z.; Zhou, Y.-N.; Lu, J. Whole-Voltage-Range Oxygen Redox in P2-Layered Cathode Materials for Sodium-Ion Batteries. *Adv. Mater.* **2021**, 33, No. 2008194.
- (59) Mao, Q.; Yu, Y.; Wang, J.; Zheng, L.; Wang, Z.; Qiu, Y.; Hao, Y.; Liu, X. Mitigating the P2–O2 Transition and Na⁺/Vacancy Ordering in Na_{2/3}Ni_{1/3}Mn_{2/3}O₂ by Anion/Cation Dual-Doping for Fast and Stable Na⁺ Insertion/Extraction. *J. Mater. Chem. A* **2021**, *9*, 10803–10811.
- (60) Veerasubramani, G. K.; Subramanian, Y.; Park, M.-S.; Senthilkumar, B.; Eftekhari, A.; Kim, S. J.; Kim, D.-W. Enhanced Sodium-Ion Storage Capability of P2/O3 Biphase by Li-Ion Substitution into P2-Type $Na_{0.5}Fe_{0.5}Mn_{0.5}O_2$ Layered Cathode. *Electrochim. Acta* **2019**, 296, 1027–1034.
- (61) Wang, M.; Wang, Q.; Ding, X.; Wang, Y.; Xin, Y.; Singh, P.; Feng, W.; Gao, H. The Prospect and Challenges of Sodium-Ion Batteries for Low-Temperature Conditions. *Interdiscip. Mater.* **2022**, 1, 373–395.
- (62) Li, Y.; Zhao, Y.; Feng, X.; Wang, X.; Shi, Q.; Wang, J.; Wang, J.; Zhang, J.; Hou, Y. A durable P2-type layered oxide cathode with superior low-temperature performance for sodium-ion batteries. *Sci. China Mater.* **2022**, *65*, 328–336.